Phantom-based study exploring the effects of different scatter correction approaches on the reconstructed images generated by contrast-enhanced stationary digital breast tomosynthesis

Connor Puett,[a] Christina Inscoe,[b] Yueh Z. Lee,[a,b,c] Otto Zhou,[a,b] and Jianping Lu[b,*]
[a]University of North Carolina at Chapel Hill, UNC/NCSU Joint Department of Biomedical Engineering, Chapel Hill, North Carolina, United States
[b]University of North Carolina at Chapel Hill, Department of Physics and Astronomy, Chapel Hill, North Carolina, United States
[c]University of North Carolina at Chapel Hill, Department of Radiology, Chapel Hill, North Carolina, United States

Abstract. Stationary digital breast tomosynthesis (sDBT) is an emerging technology in which the single rotating x-ray tube is replaced by a fixed array of multiple carbon nanotube-enabled sources, providing a higher spatial and temporal resolution. As such, sDBT offers a promising platform for contrast-enhanced (CE) imaging. However, given the minimal enhancement above background with standard operational tube settings and iodine dosing, CE breast imaging requires additional acquisition steps to isolate the iodine signal, using either temporal or dual energy subtraction (TS or DES) protocols. Also, correcting for factors that limit contrast is critical, and scatter and noise pose unique challenges during tomosynthesis. This phantom-based study of CE sDBT compared different postacquisition scatter correction approaches on the quality of the reconstructed image slices. Beam-pass collimation was used to sample scatter indirectly, from which an interpolated scatter map was obtained for each projection image. Scatter-corrected projections provided the information for reconstruction. Comparison between the application of different scatter maps demonstrated the significant effect that processing has on the contrast-to-noise ratio and feature detectability (d') in the final displayed images and emphasized the critical importance of scatter correction during DES. © *2018 Society of Photo-Optical Instrumentation Engineers (SPIE)* [DOI: 10.1117/1.JMI.5.1.013502]

1 Introduction

Now recognized clinically as three-dimensional (3-D) mammography, digital breast tomosynthesis (DBT) is a low-dose x-ray modality capable of capturing some depth information by collecting a series of oblique two-dimensional (2-D) projection views from which a 3-D image space is mathematically reconstructed for viewing. Experience with currently approved DBT devices suggests an improved detection of breast masses and a lower call-back rate for false-positive findings when DBT is combined with standard digital mammography for screening, especially in the setting of a high fibroglandular content.[1–6] Additionally, DBT is being explored as a diagnostic tool for evaluating suspicious breast lesions, with studies comparing its performance with other imaging modalities capable of providing 3-D information, including computed tomography, ultrasound, and magnetic resonance (MR).[7–10] In each of these, contrast-enhanced (CE) imaging has been used to improve diagnostic accuracy, with a goal of exploiting the altered vasculature of malignant tissue. However, at this time, the most appropriate role for DBT has yet to be defined, in part given concern over the diagnostic accuracy when characterizing microcalcifications, a key feature in the differentiation of benign from malignant breast lesions. Characterizing microcalcifications requires a high system resolution, and the resolution of currently approved DBT devices is lower than digital mammography, given the problems of noise, scatter, and blur unique to tomosynthesis.[11]

Noise, scatter, and blur pose unique challenges during DBT. Additionally, these challenges tend to be magnified during CE imaging, given the need for higher photon energies, the presence of the highly attenuating contrast agent, and the critical importance of minimizing factors that decrease contrast. During DBT, the x-ray dose used during mammography to collect a single cranial-caudal (CC) or mediolateral oblique view is divided among the multiple projections. Currently approved DBT devices collect between 9 and 25 projections per scan.[12] As such, the relative contribution of noise to the total signal in each projection image is higher during DBT compared with mammography. Scatter is problematic for all x-ray based imaging. In response, air-gaps and antiscatter grids are used to limit the chance that a photon following an oblique path, and therefore more likely to have been deflected from its primary path, will reach the detector. However, tomosynthesis requires the collection of oblique projections; as such, static antiscatter grids and large air-gaps are usually avoided, although one commercial DBT system has successfully incorporated an antiscatter grid.[13] Blur artifact related to both patient and source motion can be problematic during tomosynthesis. Currently approved DBT

---

*Address all correspondence to: Jianping Lu, E-mail: jpl@email.unc.edu

devices swing a standard x-ray tube through space to collect the series of projection views, either in a continuous or step-and-shoot motion. Although the step-and-shoot approach avoids the problem of source blur inherent with continuous motion imaging, it takes more time, increasing the chance that the patient will move.[14] Ongoing research into both the technology of image acquisition and postacquisition image processing is addressing these challenges. The development of stationary DBT (sDBT) is an example of this advancing technology.

sDBT offers a higher spatial and temporal resolution than the rotating-source DBT devices currently in clinical use.[15,16] The improved performance is made possible by a unique x-ray tube design, which consists of a distributed and fixed array of carbon nanotube (CNT)-enabled x-ray sources.[17] CNT cathodes release the electrons needed for x-ray generation at room temperature and essentially instantaneously. Hence, arrays of multiple CNT-enabled sources can be aligned, and their x-ray emissions can be coordinated. A motion-free series of projection views can thereby be obtained quickly, providing an ideal solution to the technical limitations of rotating-source DBT. The electrons are directed toward a standard metal anode, producing an x-ray spectrum of photon number and energies similar to standard imaging devices and allowing for a rapid translation to clinical use. X-ray devices for breast, chest, and dental imaging have been developed with CNT technology and are being tested in Institutional Review Board-approved studies.[18–20]

To date, most clinical experience with 3-D CE breast imaging has been with gadolinium-enhanced MR.[21] However, given the high cost and limited availability of MR compared with radiation-based imaging, research continues into the development of CE DBT. For radiation-based techniques, such as DBT, iodine is the contrast agent of choice. However, CE mammography has shown only a minimal lesion enhancement above background (BKG) following standard intravenous iodine dosing and has demonstrated that the differences distinguishing benign from malignant enhancement patterns in breast lesions are subtle.[22] As a result, two imaging steps with subtraction are needed for CE mammography and CE DBT. Subtraction removes the BKG signal and thereby improves contrast in the enhanced tissue. These experiments simulated both temporal subtraction (TS) and dual-energy subtraction (DES) protocols. TS involves imaging before and after the administration of contrast using a photon energy above the characteristic absorption (K-edge) for iodine, whereas DES compares images collected with photon energies above and below the K-edge.[23] Although this critical subtraction step during CE imaging has been studied for rotating-source DBT previously, this work is the first to incorporate scatter correction with a stationary system.[24,25]

Tomosynthesis displays its findings as a stack of reconstructed image slices through which the reader scrolls to identify pathology and appreciate depth relationships. In large part, the diagnostic utility of this image stack depends on the effectiveness by which postacquisition image processing steps correct for the noise, scatter, and artifact problems inherent with DBT. Comparison studies are important, as manipulating the information in the 2-D projection image can have a significant impact on the quality of the mathematically generated (reconstructed) 3-D image space. The purpose of this study was therefore to explore different scatter correction approaches in a phantom-based model of CE sDBT. The findings are a step toward the potential clinical application of sDBT for CE imaging, and they highlight the importance of scatter correction for tomosynthesis image presentation in general.

2 Materials and Methods

2.1 Customizing the Breast Phantom

The 1-cm thick slabs of the CIRS (Norfolk, Virginia) model 020 BR3D breast phantom were stacked to create compressed breast thicknesses of 3, 4, and 5 cm. The phantom mimicked a breast environment with 50% fatty and 50% fibroglandular tissue in a swirled pattern most similar to BI-RADS heterogeneous or type 3 density. Contrasted lesions were simulated by wells drilled in a 1-cm thick acrylic plate that had attenuation similar to the breast phantom. The 2.5-mm deep wells had diameters of 0.5, 1, 1.5, and 2 cm and were filled with iodinated contrast (iohexol) diluted with water to concentrations of 0, 1, 2.5, 5, 10 and 15 mg/mL and capped to remove any overlying air. Contrast concentrations in imaging studies are often reported as area densities to allow correlation with signal intensities over a defined area in the image. The area densities in this study ranged from 0 to 3.75 mg/cm^2, reproducing those reported in clinical trials of CE mammography.[22] The acrylic plate was positioned between the two phantom slabs closest to the detector [Fig. 1(b)].

2.2 Acquiring the Images

The sDBT system[16] consisted of a CNT-enabled linear x-ray source array (XinRay Systems, Inc.) that was retrofitted to a Hologic Selenia Dimensions DBT unit and positioned to collect a standard CC view [Fig. 1(a)]. Based on previous testing to optimize the geometry of the system, 19 projection images were acquired for each scan, over an angular span of 35 deg at a source-to-detector distance of 81 cm. Electron emission from CNT cathodes is voltage-controlled, which was automatically adjusted by an electronic control system to maintain the desired operational tube settings. Since the x-ray on-time of the imaging system used in these experiments was limited to
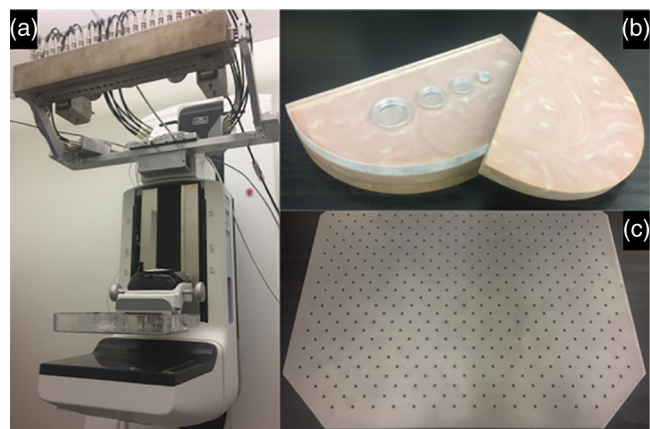
Fig. 1 The experimental equipment. (a) The sDBT device was a modified Hologic Selenia Dimensions DBT unit in which the single rotating x-ray source was replaced with a fixed array of multiple CNT-enabled x-ray sources. (b) The breast phantom was customized to include acrylic wells reproducing a range of tumor sizes into which clinically appropriate iodine concentrations were added. (c) The primary sampling device was a steel sheet containing 2-mm holes spaced 10.6-mm apart and positioned just above the upper compression plate for imaging.

60 ms, each of the 19 sources was driven three times at a tube current of 25.8 mA and the corresponding projections were summed, resulting in a total exposure of 88 mA. The intent was to replicate typical tube settings used in the clinic. The tube voltage and, thus, maximum photon energy was set at 49 kVp for TS and high-energy (HE) DES imaging, while 30 kVp was used to collect the low-energy (LE) DES images. A 0.25-mm copper filter was added to the standard 0.5 mm aluminum filter during HE imaging to remove photons with energies below the iodine K-edge (33.2 keV).

The average nominal anode focal spot size was 1.1 mm, and, as operated in these experiments, the system resolution corresponding to the frequency at 10% of the normalized MTF was 5.4 cycles/mm.[16] The breast compression equipment and digital detector remained original to the Hologic Selenia Dimensions system, which was operated without an antiscatter grid. The a-Se direct conversion detector had a field-of-view 29×24 cm and was operated in a 2×2 binned mode with an effective detector pixel size of 140×140 μm, which also defines the size of the projection image pixel.

2.3 Measuring Scatter

In these experiments, scatter was measured indirectly using a beam-pass primary sampling device (PSD) to sample the primary component of the total signal.[26] The protocol involved collecting a second series of 19 projection images immediately after the initial scan with the PSD positioned on the compression plate between the phantom and x-ray source. The PSD was a 2-mm thick stainless-steel sheet with 2-mm diameter holes separated by a center-to-center distance of 10.6 mm [Fig. 1(c)], resulting in an average of 118 holes located over the phantom. By comparing the total area of the PSD holes with the area of the breast phantom, it was determined that collecting the second series of projections with the PSD in place added an average of 3% of the radiation dose delivered during imaging without the PSD.

Images collected with the PSD contained circular regions of signal against a low signal BKG. In these experiments, signal was defined simply as the average of the pixel intensity values in the normalized projection image (see Sec. 2.4.1) or reconstructed image slice within a defined region-of-interest (RoI) and was reported in gray-scale units. The PSD-collimated projection images were binarized by thresholding, and the circular regions were isolated based on their known size. These regions consisted of a central plateau of primary photons and a ring of penumbra. The central pixel was identified for each region, and the signal within a 3-pixel radius around the central pixel was defined as $\mathrm{signal_{primary}}$. $\mathrm{Signal_{scatter}}$ was calculated as the difference between $\mathrm{signal_{primary}}$ and $\mathrm{signal_{total}}$, which was the signal in the same region of the corresponding projection image obtained without the PSD:

$$\mathrm{Signal_{scatter}} = \mathrm{Signal_{total}} - \mathrm{Signal_{primary}}. \qquad (1)$$

Interpolation was used to assign information regarding scatter to pixels located between these sampled regions. The result was a scatter "map" unique to each projection image. In this study, different algorithms for developing the scatter map were compared (see Sec. 2.4.2).

2.4 Postacquisition Processing and Reconstruction

2.4.1 Image processing chain and computational costs

Postacquisition processing refers to the computational steps by which information available from a set of 2-D projection views is modified prior to reconstruction. In tomosynthesis, the processing and reconstruction steps generate a stack of image slices that displays the object space in 3-D. The goal is to assign gray-scale values to the reconstructed image slices that reflect the actual attenuation in the same region of the imaged object. Beer's law describes the mathematical relationship between the x-ray beam intensity and attenuation. It relates attenuation to the negative natural log of the ratio of the x-ray intensity behind the object to the incident x-ray intensity. This ratio is determined experimentally by comparing the pixel values of projections taken with the object in-place ($\mathrm{signal_{raw}}$) with pixel values obtained using an equivalent exposure but no object ($\mathrm{signal_{blank}}$). The first computational step in these experiments was therefore to determine a normalized projection image, which is the ratio of raw to blank pixel values, corrected for detector offset and nonfunctioning pixels by subtracting averaged pixel values from 30 dark images obtained without fired x-rays ($\mathrm{signal_{dark}}$):

$$\mathrm{Signal_{normalized}} = \frac{\mathrm{Signal_{raw}} - \mathrm{Signal_{dark}}}{\mathrm{Signal_{blank}} - \mathrm{Signal_{dark}}}. \qquad (2)$$

Second, these normalized projection images were scatter-corrected by applying the different scatter maps (see Sec. 2.4.2). Third, to obtain the TS and DES projection image, the pair of normalized and scatter-corrected projection images generated by each source was combined using a weighted logarithmic subtraction step. The weighting factor was derived mathematically for each projection image pair as the scalar resulting in maximum cancellation of the average BKG signal.[27] Fourth and finally, the information from these projection images, now containing pixel values manipulated by normalization, scatter correction, and subtraction, was used as the input for reconstruction by an iterative approach (see Sec. 2.4.3). The result was a reconstructed stack of image slices separating the image space in 0.5-mm depth increments. Seeing the images allows appreciation of the signal changes that occur through the postacquisition processing steps of subtraction and then reconstruction. Figure 2 displays this image progression, using representative examples from TS and DES protocols without scatter correction. In these protocols, 76 projection images were collected to generate the reconstructed image stack. For example, the TS protocol began by collecting 38 projection images (19 with and 19 without the PSD) before contrast and then repeating the same series of projections when contrast was present. The same number of projection images was acquired for DES, although images were obtained using low and high photon energies when contrast was present. All image processing code was written in MATLAB. The total computation time to move through the process from projection view normalization, scatter map development and application, subtraction, and finally reconstruction was 18.25 min, using an off-the-shelf four-core MacBook Pro with a 2.7 GHz Intel Core i5 processor. The total computation time was reduced to 11 min using a six-core 3.5 GHz Intel Core i7 processor and could be reduced further by implementing the code in C programming language and using GPU parallel processing.
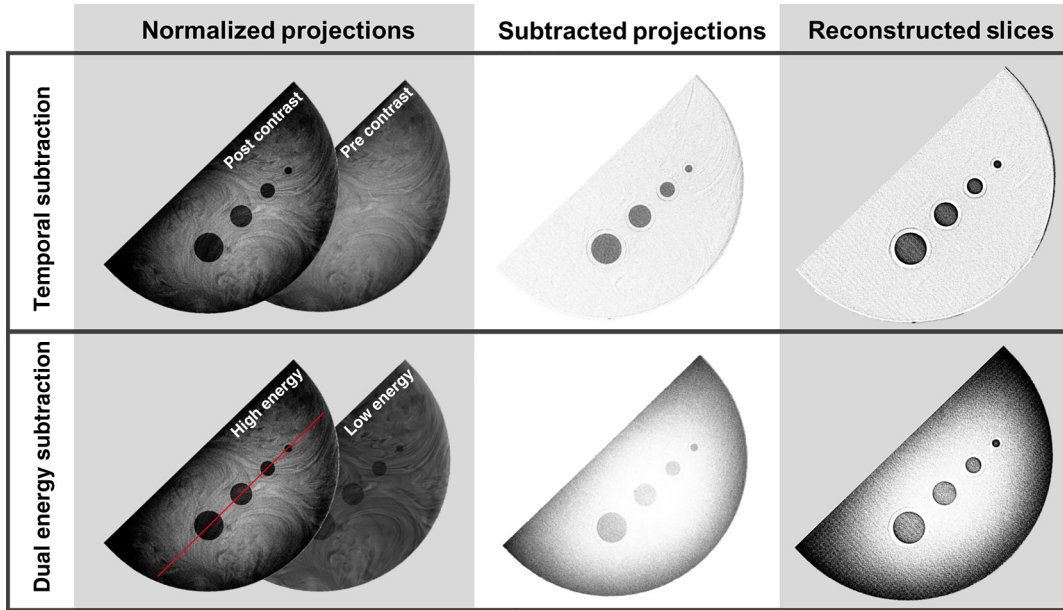
Fig. 2 Representative images through the postacquisition processing steps. In these examples, temporal subtraction (TS) and dual energy subtraction (DES) protocols were used to collect projection views of a 5-cm thick phantom containing iodine at a concentration of 15 mg/mL. Note the "cupping" artifact, which refers to the intensity differences between the periphery and central regions of the image, present in the high energy normalized projections and persisting in processed DES images without scatter correction. The red line through the high-energy DES normalized projection image identifies the line profile path presented in Fig. 6.

2.4.2 *Scatter correction*

Correcting for scatter is the mathematical step of adjusting pixel values to remove the scatter component from the total signal. Typically, this correction is made at the level of the projection image prior to reconstruction and involves applying a map of pixel-specific scatter values to the projection image. However, different algorithms have been proposed in the literature to generate the scatter map, based on applying direct scatter values[28,29] or values incorporating the scatter-to-primary ratio (SPR).[30] In this study, three approaches for generating pixel-specific scatter maps, referred to as ScatterMap$_{direct}$, ScatterMap$_{SPR}$, and ScatterMap filtered-SPR (ScatterMap$_{fSPR}$), were compared.[31] Each approach differed in its application of information collected by beam-pass collimation (see Sec. 2.3).

ScatterMap$_{direct}$ was simply a biharmonic spline interpolation [Eq. (3)] of signal$_{scatter}$ [Eq. (1)] determined at the PSD-sampled sites:

$$\mathrm{ScatterMap}_{direct} = \mathrm{Interpolation}(\mathrm{Signal}_{scatter}). \quad (3)$$

Developing ScatterMap$_{SPR}$ was a three-step process. First, SPR was calculated at the PSD-sampled sites [Eq. (4)]. Second, biharmonic spline interpolation assigned SPR values to pixels between the PSD-sampled sites [Eq. (5)]. The final step [Eq. (6)] calculated a pixel-specific scatter value from SPR$_{interp}$ to generate ScatterMap$_{SPR}$:

$$\mathrm{SPR}_{sampled} = \left(\frac{\mathrm{Signal}_{scatter}}{\mathrm{Signal}_{primary}}\right), \quad (4)$$

$$\mathrm{SPR}_{interp} = \mathrm{Interpolation}(\mathrm{SPR}_{sampled}), \quad (5)$$

$$\mathrm{ScatterMap}_{SPR} = \mathrm{Signal}_{total} * \frac{\mathrm{SPR}_{interp}}{1 + \mathrm{SPR}_{interp}}. \quad (6)$$

The mathematical steps to develop ScatterMap$_{fSPR}$ can be considered a blend of the calculations used to generate the direct and SPR maps described above. First, an SPR$_{direct}$ value was calculated for every pixel using ScatterMap$_{direct}$ and Signal$_{total}$ [Eq. (7)]. As such, SPR$_{direct}$ differed from SPR$_{interp}$ in terms of the information that was interpolated from the PSD-sampled sites to pixels between the sampled sites. Next, a scatter value was assigned to each pixel using a mathematical step similar to Eq. (6). However, developing ScatterMap$_{fSPR}$ included the application of a 2-D Gaussian filter (f) to SPR$_{direct}$ [Eq. (8)]:[23]

$$\mathrm{SPR}_{direct} = \frac{\mathrm{Scatter}_{direct}}{\mathrm{Signal}_{total} - \mathrm{Scatter}_{direct}}, \quad (7)$$

$$\mathrm{ScatterMap}_{fSPR} = \mathrm{Signal}_{total} * \frac{f\mathrm{SPR}_{direct}}{1 + f\mathrm{SPR}_{direct}}. \quad (8)$$

A scatter map refers to the collection of all pixel-specific scatter values. Correcting the normalized projection image signal (Signal$_{corrected}$) for scatter was accomplished by simple subtraction [Eq. (9)]:

$$\mathrm{Signal}_{corrected} = \mathrm{Signal}_{total} - \mathrm{ScatterMap}_{direct \, or \, SPR \, or \, fSPR}. \quad (9)$$

2.4.3 *Reconstruction*

Reconstruction refers to the computational steps that use 2-D information available from the processed projection images to

generate a 3-D image space mathematically for viewing. Great variation now exists in the digital processing available to accomplish reconstruction, and research continues to optimize reconstruction for tomosynthesis. However, reconstruction approaches can be classified generally into broad categories, based on the mathematical steps that move information between the 2-D projection and 3-D image spaces. This study used an iterative approach similar to the simultaneous iterative reconstruction technique, customized to the unique geometry of the sDBT system.[32] The algorithm started with uniform image space values and performed 20 iterations.

2.5 Measuring Image Quality and Feature Detectability

The contrast and the contrast-to-noise ratio (CNR) were chosen as the primary measures of image quality since they quantify the key image characteristics that determine visibility during CE studies. These measurements were made in the central regions of the breast, as this area is known to be most affected by cupping artifact from scatter. The effect of cupping on the image can be appreciated by comparing the representative TS and DES images in Fig. 2. Noise (σ) was measured as the standard deviation in the BKG signal, with BKG RoIs placed adjacent to the iodine-containing region (iRoI). Contrast was calculated as the difference between the signal in an iRoI and its BKG signal [Eq. (10)], while the CNR was calculated as the ratio of the contrast to σ_{BKG} [Eq. (11)]:

$$\text{Contrast} = \text{Signal}_{\text{iRoI}} - \text{Signal}_{\text{BKG}}, \tag{10}$$

$$\text{CNR} = \frac{\text{Contrast}}{\sigma_{\text{BKG}}}. \tag{11}$$

Circular regions with half the diameter of the iodine wells were used for calculating signal and noise in iRoI and BKG, and all measurements for contrast and CNR calculations were made at the level of the reconstructed image slice, generated from projection image pairs following normalization (log transformation), subtraction, and scatter correction (see Sec. 2.4.1).

However, manipulating pixel values through image processing, such as the application of scatter correction algorithms, often involve trade-offs in contrast, noise, and resolution. Characterizing mass margins as well as the appearance and distribution of microcalcifications is clinically important and requires maintaining image resolution. Therefore, as an additional measure of image quality, a modified feature detectability index (d') was used to compare images generated using the different scatter correction approaches. d' integrates resolution, contrast, and noise as they relate to a specific task.[24] In this study, resolution was defined by the task transfer function measured off the contrasted-well edge in the in-focus image slice reconstructed from HE projection images without scatter correction and following the application of ScatterMap$_{\text{direct}}$, ScatterMap$_{\text{SPR}}$, or ScatterMap$_{f\text{SPR}}$. The noise power spectrum was calculated using BKG, and contrast was calculated as described in Eq. (10).

2.6 Coding and Statistical Analysis

Coding was done in MATLAB and ImageJ. Datasets were evaluated by t-test for paired comparison or one-way analysis of variance (ANOVA) to compare multiple groups. All results

are reported as the mean of the data and its corresponding standard deviation with p values of <0.05 considered to be statistically significant. Linear relationships were assessed using the coefficient of determination (R^2).

3 Results

3.1 Scatter

In projection images, the relative contribution of scatter to the total signal, quantified by SPR, was higher in iRoI compared with BKG (Fig. 3). In part, this finding resulted from attenuation differences between the water filling the wells and the surrounding acrylic since iRoI SPR was similar over the range of iodine concentrations [Figs. 4(a) and 4(b)]. The results demonstrated a strong correlation between SPR and phantom thickness when measured in both iRoI [Figs. 4(a) and 4(b)] and BKG [Figs. 4(c) and 4(d)]. Finally, SPR tended to be higher in images collected at a higher photon energy. Analysis of these trends demonstrated a greater increase in scatter relative to the primary signal.

These experiments compared different scatter correction algorithms on image quality, utilizing scatter maps based on sampled scatter values (ScatterMap$_{\text{direct}}$), calculated SPR values (ScatterMap$_{\text{SPR}}$), or a filtered combination of both (ScatterMap$_{f\text{SPR}}$) (see Sec. 2.4.2). The maps differed in their representations of scatter (Fig. 5). Only maps including an SPR calculation [Figs. 5(b) and 5(c)] captured the noise component of the scatter signal. Therefore, unlike ScatterMap$_{\text{SPR}}$ and ScatterMap$_{f\text{SPR}}$, ScatterMap$_{\text{direct}}$ was smooth [Fig. 5(a)]. Additionally, given the relatively sparse sampling by the PSD and the chance that an iodine-containing well was not adequately sampled, ScatterMap$_{\text{SPR}}$ tended to assign lower scatter values to regions of high attenuation [Fig. 5(b)] compared with ScatterMap$_{\text{direct}}$, potentially underestimating scatter in areas of the image where there was a rapid change in the primary signal. The fSPR algorithm was designed to generate a scatter map that blended the most useful qualities of both ScatterMap$_{\text{direct}}$ and ScatterMap$_{\text{SPR}}$.[31,33] Figure 6 displays the effect of applying the different scatter maps on the projection image. It superimposes two line profiles. The colored profiles display the changing signal through the center of iodine-containing wells in representative projection images adjusted by the different scatter correction techniques. The black profiles reflect the same path through the applied scatter map. The application of each map corrected the cupping artifact, which refers to the signal difference in central breast regions compared with the periphery. Additionally, the application of maps developed using an SPR calculation [Figs. 6(c) and 6(d)] generated a smoother projection image compared with the application of ScatterMap$_{\text{direct}}$ [Fig. 6(b)].

3.2 Effects of Different Scatter Correction Approaches on Image Quality and Feature Detectability

3.2.1 Contrast and the contrast-to-noise ratio

The postacquisition processing steps of weighted subtraction and scatter correction were specifically designed to isolate the iodine signal by minimizing the BKG signal. As such, the analysis focused on appreciating the effect of different scatter correction approaches on the relationships between image quality and the concentration of iodine, using averaged data
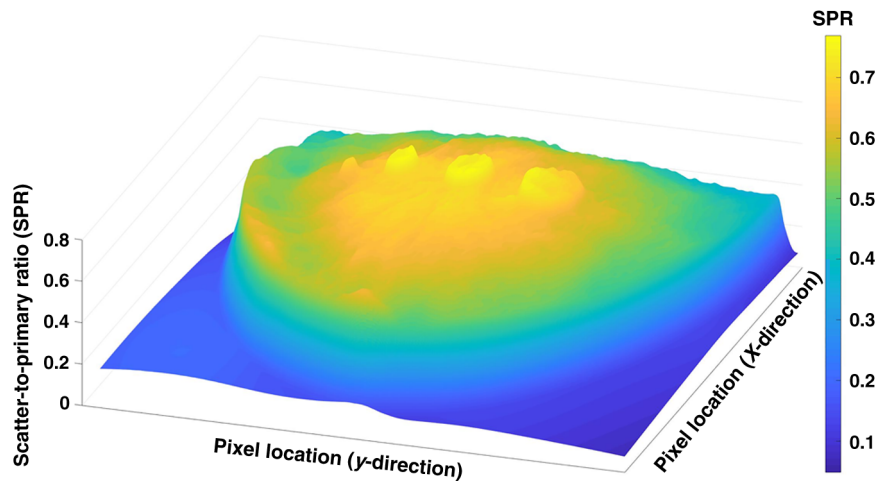
Fig. 3 SPR values in a representative projection image. In this example, the 5-cm thick phantom contained iodine at a concentration of 15 mg/ml and was imaged at 49 kVp. Note the higher SPR values in regions of iodine-containing wells.
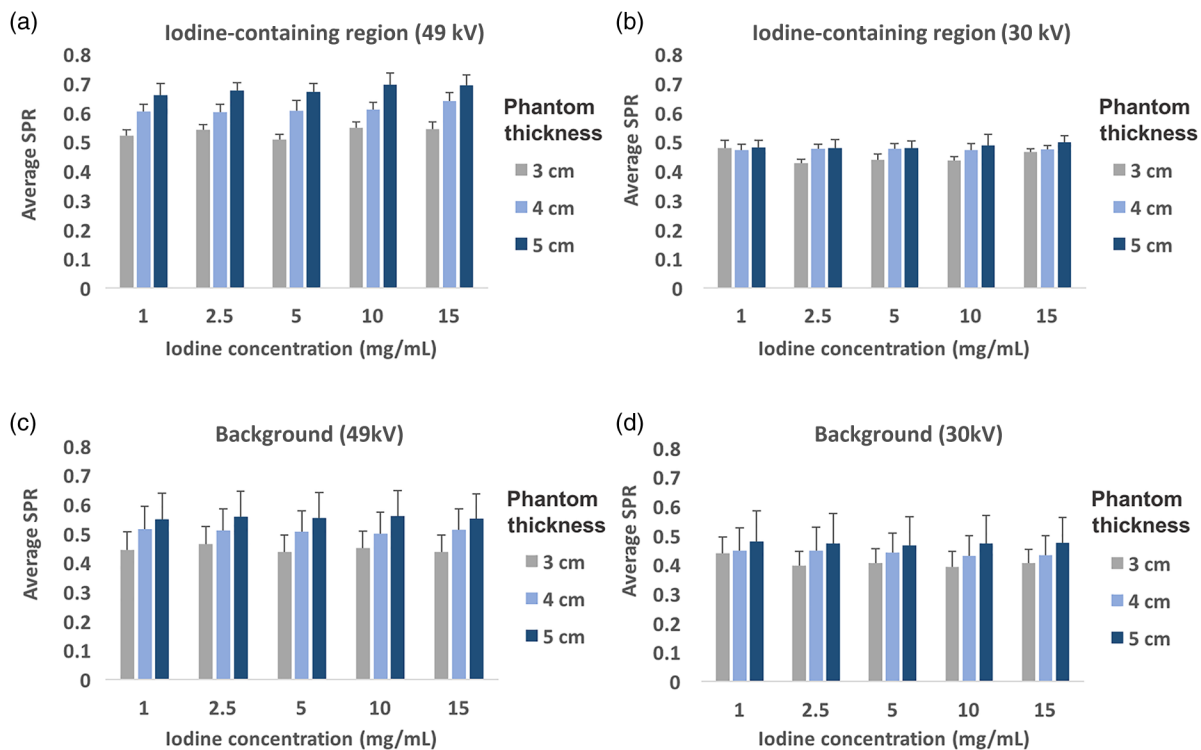
Fig. 4 The SPR as a function of iodine concentration and breast thickness in projection images collected using high (49 kVp) and low (30 kVp) photon energies. SPR was dependent on phantom thickness ($p < 0.05$ by ANOVA in BKG) and tended to be higher when images were collected at higher photon energy.

from all well sizes and breast thicknesses for each iodine concentration. Two important relationships were noted when contrast and CNR in the iRoIs of reconstructed images were assessed as a function of iodine concentration. Figure 7 compares these relationships for images collected using TS and DES protocols. First, there was a strong linear correlation ($R^2 \geq 0.97$) between contrast and CNR with the iodine concentration. Second, contrast and CNR were higher in images collected using the TS protocol compared with DES for all iodine concentrations.

Figure 8 summarizes the effects of applying the different scatter correction algorithms on contrast and the CNR in the reconstructed image slices. There are several observations. Scatter correction by all three methods improved contrast when projection images were collected using the TS protocol. During DES, this increase in contrast was statistically significant for all iodine concentrations. Unlike contrast, CNR includes a measure of noise. Hence, as expected, the application of SPR-based scatter maps, which capture the noise component of the scatter signal, tended to yield higher CNR values
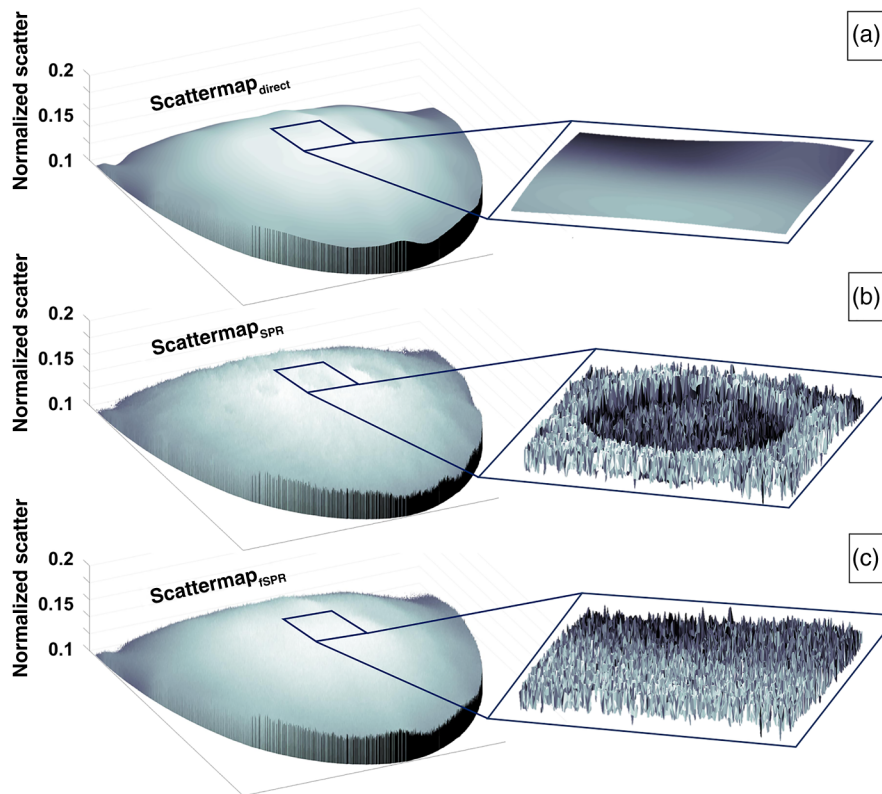
Fig. 5 Representative maps developed using either (a) direct scatter values (ScatterMap$_{direct}$), (b) an SPR calculation (ScatterMap$_{SPR}$), or (c) a filtered combination of both (ScatterMap$_{fSPR}$). These examples were generated when a 5-cm thick phantom containing iodine at a concentration of 15 mg/ml was imaged at 49 kVp. The expanded views highlight differences in the region of the 1.5-cm diameter well. Note the noise component present in the scatter maps containing an SPR component, compared with the smooth direct scatter map. Also, note the lower scatter values assigned to the well region by the SPR map relative to the other maps.

compared with no scatter correction or the application of a direct scatter map. Additionally, for both TS and DES, only the fSPR scatter correction algorithm significantly increased CNR above the no scatter correction value for all iodine concentrations. In fact, for the DES protocol, applying the fSPR scatter correction algorithm yielded CNR > 1 at an iodine concentration of 5 mg/ml. Without scatter correction, an iodine concentration of at least 10 mg/ml was required to achieve CNR > 1. CNR values > 1 indicate that the difference between the iodine signal and its BKG is greater than the BKG noise. As such, the contrasted region should be visible to a reader.

3.2.2 Feature detectability

d' values were lower with DES compared with TS for all iodine concentrations. However, there was no loss in feature detectability with the application of scatter correction algorithms compared with no scatter correction for TS or DES (Fig. 9). Additionally, similar to the trend with CNR, scatter correction using SPR and fSPR tended to yield higher d' values than direct scatter correction, suggesting that the incorporation of a noise component into the scatter correction algorithm did not significantly compromise resolution. Overall, the fSPR scatter correction approach tended to yield the highest d' values.

4 Discussion

Research continues to define the most appropriate tools to detect, evaluate, and monitor breast lesions. Appropriateness reflects a balance of utility, availability, cost, and risk. As such, there is no ideal solution, and studies are evaluating the performance of both transmission (x-ray and ultrasound) and emission (radiopharmaceutical) imaging as well as MR. Indeed, some approaches are more useful in certain circumstances than others. However, in general, studies have supported that it is better to collect 3-D information than 2-D information and that enhanced 3-D imaging is better than nonenhanced imaging during the diagnostic evaluation of suspicious breast lesions.[9] Now recognized as 3-D mammography, DBT is a low-cost and low-dose x-ray modality with a rapidly expanding availability for clinical use. Hence, studies exploring the potential of CE DBT are being conducted. sDBT is an experimental technology, in which multiple CNT-enabled x-ray sources are aligned, providing a fixed architecture capable of capturing a wide span of projection views quickly. As such, sDBT offers a higher spatial and temporal resolution than currently available DBT devices,[15,16] which must rotate a standard x-ray source through the angle span. As such, sDBT may provide a useful platform for CE imaging, and a previous report has documented the ability of this sDBT system to collect images using TS and DES protocols.[33] The purpose of this phantom-based study was to explore the use of different postacquisition image processing approaches during CE sDBT, given the fact that scatter and noise pose unique challenges during DBT that require correction, especially when DBT is applied to environments containing highly attenuating features.
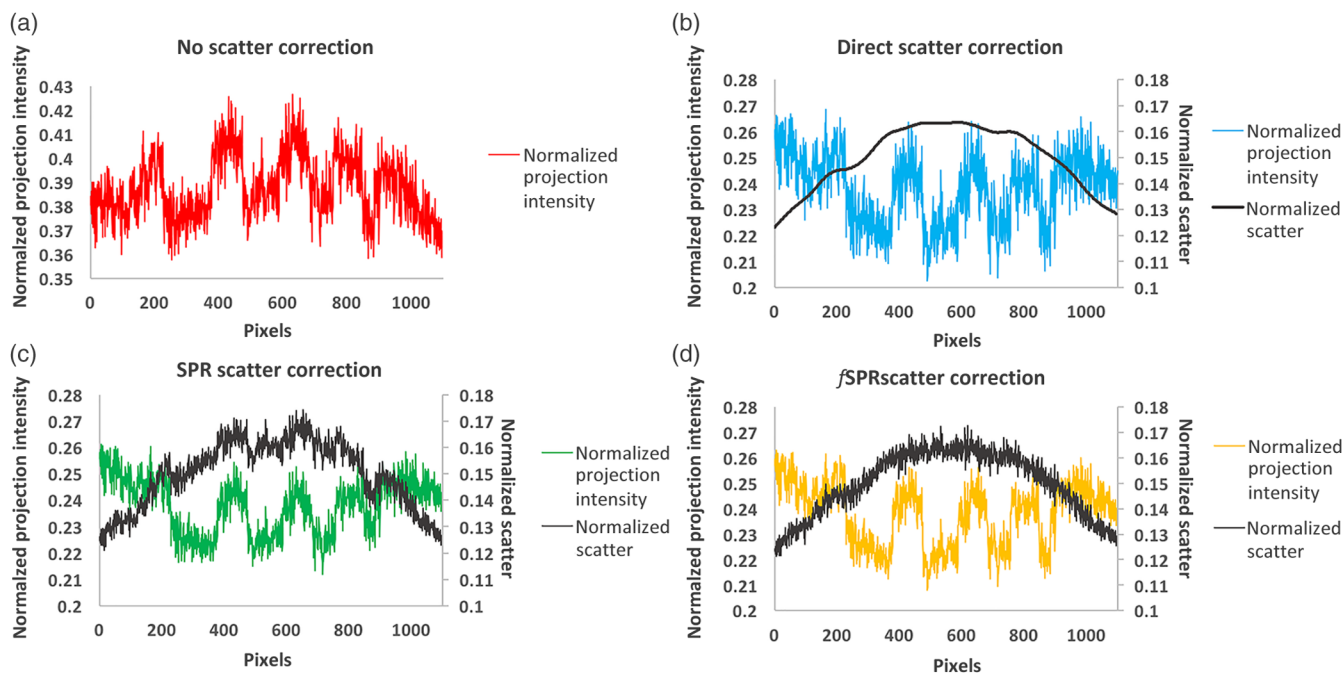
Fig. 6 Line profiles through a representative projection image (colored profiles) and the three scatter maps (black profiles) that were applied to it. (a) No scatter correction, (b) direct scatter correction, (c) SPR scatter correction, and (d) filtered SPR (fSPR) scatter correction. All projection images were normalized to a blank scan, as described by Eq. (2). Note the different y-axis scales of signal intensity for the projection image and scatter map. These line profiles correspond to the iodine-containing high energy normalized projection image shown in Fig. 2 (lower left corner red line) and the scatter maps shown in Fig. 5. Note the inverted "cup-shape" of the noncorrected projection profile and scatter profiles. (c and d) captured the noise component of the scatter signal and therefore yielded a smoother scatter-corrected image.
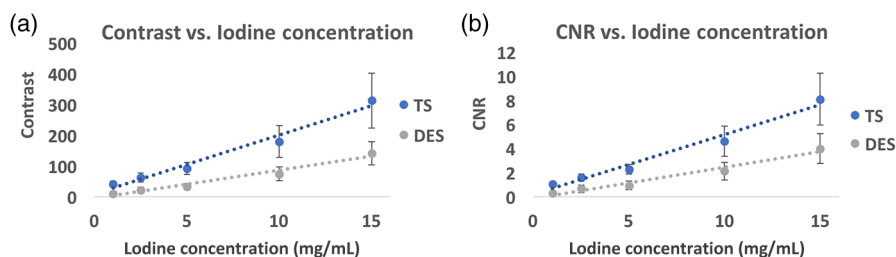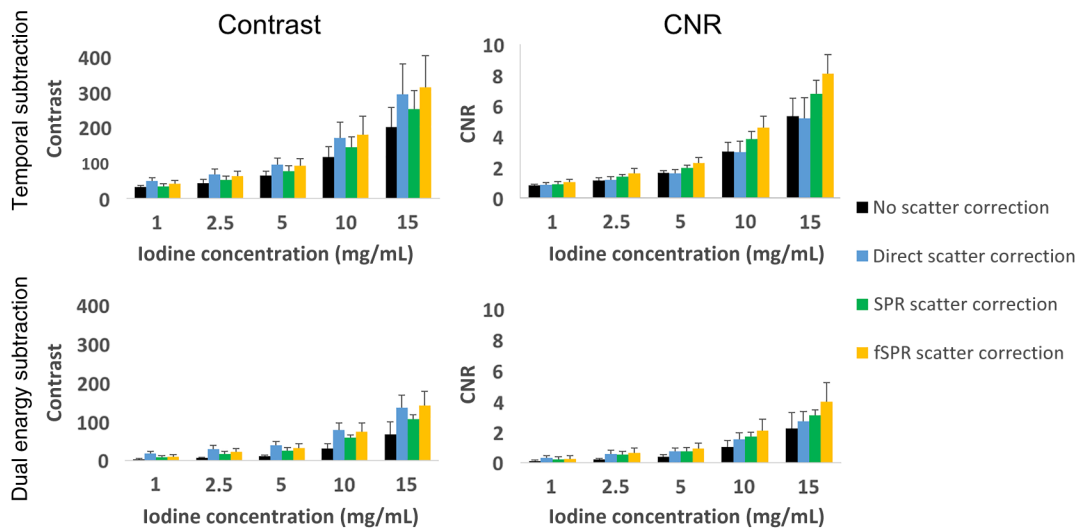

Fig. 7 (a) Contrast and (b) the CNR as functions of iodine concentration in reconstructed image slices. These representative data compare TS and DES protocols with scatter correction using an fSPR map. Similar trends were seen with the other scatter correction approaches.

This study investigated the effects of different scatter correction approaches on contrast and noise. The direct scatter correction approach maintained good contrast but did not account for the noise component of the scatter. Scatter correction based on SPR did account for noise but compromised contrast. fSPR can be considered a blend of the direct and SPR scatter approaches and was designed to maximize the beneficial attributes of each.[31] Indeed, in this study, scatter correction using fSPR yielded the highest observed values for CNR for both TS and DES protocols. Importantly, this increase in CNR was achieved without compromising resolution, as demonstrated by the fact that applying fSPR also yielded images with the highest feature detectability, quantified using an index incorporating a task-based measure of resolution.

There were significant differences in the quality of the images produced using TS and DES images. TS yielded images

with higher CNR and d' than DES for all iodine concentrations. Additionally, with the TS protocol, an adequate CNR was achieved for most iodine concentrations regardless of the post-acquisition processing approach. However, in looking toward a potential clinical application, TS is more problematic than DES from a practical standpoint. TS protocols involve collecting a set of views, delivering an IV contrast bolus, and then waiting at least 2 min before collecting a second set of views.[34] In this scenario, accomplishing an accurate subtraction step between the pre- and postcontrast images, either at the level of the projection image or reconstructed image slice, can be problematic since it requires the registration of images collected after two separate breast compressions. Compression introduces unpredictable variability in the location of anatomic features. DES is preferable, as both image sets, one using a low photon energy and the second using a high photon energy, can be obtained after

Fig. 8 (a–d) Contrast and the CNR in reconstructed image slices as functions of iodine concentration, comparing different scatter correction algorithms when TS and DES protocols were used to collect the projection images. Scatter correction by any method improved contrast. However, for both TS and DES, only the fSPR correction algorithm produced a statistically significant increase in CNR ($p < 0.05$ by t-test) compared with no scatter correction for all iodine concentrations.
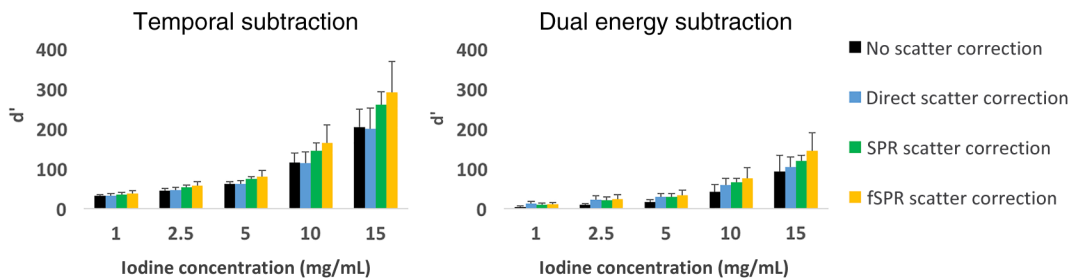
Fig. 9 The detectability index (d') in reconstructed image slices as a function of iodine concentration, comparing different scatter correction algorithms when (a) TS and (b) DES protocols were used to collect the projection images. There was no loss in feature detectability with the application of scatter correction.

the administration of contrast without interruption and during one compression. For DES, the ability to collect many images quickly is important, and, as noted above, sDBT has a high potential temporal resolution. Unlike TS, postacquisition image processing had a significant impact on the quality of images obtained by DES. Scatter correction was critical, and employing a filtered scatter correction algorithm that blended a weighted contribution of direct and SPR input yielded the highest CNR and d' in reconstructed images.

Different methods have been developed to determine the scatter signal applied to correct the projection image during DBT. Many of these tap libraries of scatter maps developed by simulation and historical measurements made on phantoms and breasts.[29,35] The maps are selected based on some anatomic features, such as breast thickness. Library-based scatter correction is appealing since additional imaging is not required at the time of the study. However, in these experiments, beam-pass collimation was used to develop a unique scatter map for every projection, as comparing different scatter correction approaches required accurate sampling of the scatter and primary signals. Additionally, measuring scatter may prove to be helpful in the clinical setting, given the unpredictable nature of contrast enhancement. The PSD collimator provides true,

patient-specific scatter information. Although collecting images with beam-pass collimation adds just minimal radiation, it does introduce the technical problem of maneuvering the PSD into position. Limiting the overall scan time is important for both patient comfort and to minimize patient motion. Although the hardware to move the PSD will need to be developed, the PSD is conveniently located just above the breast compression plate. Again, when handling the PSD, the DES protocol offers an advantage over TS, as HE and LE imaging with and without the PSD can be accomplished by moving the PSD into place just once.

Clinical experience with gadolinium-enhanced MR has shown that the diagnostic benefits of CE are found in the improved delineation of mass margins and an improved ability to appreciate the association of microcalcifications in nonmass lesions.[36,37] Additionally, the kinetics of CE may have diagnostic utility, suggesting that the ability to collect images rapidly through time may be of value.[38] Such a temporal capability is known as dynamic or four-dimensional CE. sDBT may offer a platform for radiation-based dynamic breast imaging, given its potential for a high temporal resolution. Phantoms reproducing the changing iodine concentrations seen clinically after an iodine infusion have been developed and offer an

approach to test dynamic CE sDBT.[39] Future phantom-based studies to explore DES protocols for dynamic imaging with sDBT are being planned.

Finally, the sDBT unit used for these experiments is similar to a device operating in studies assessing the diagnostic accuracy of sDBT compared with standard digital mammography in women with suspicious (BI-RADS 4 and 5) breast lesions[40] and concerning microcalcifications.[41] This patient population provides an opportunity to evaluate the feasibility and utility of the PSD-based method of scatter measurement in the clinical setting. The findings from this study support continued work along these lines. Future studies assessing the performance of the different scatter correction approaches across a range of clinically appropriate radiation doses for both noncontrasted and CE sDBT as well as the development of the hardware to deploy the PSD will be needed.

5 Conclusion

This phantom-based study of CE breast imaging using sDBT highlights the unique challenges posed by scatter during breast tomosynthesis and the significant impact that different postacquisition processing steps can have on the information available in the reconstructed images. These findings will help guide processing choices and hardware development as sDBT testing moves forward in human studies. Additionally, understanding how different postacquisition processing approaches handle scatter around features with high contrast has broader implications, as the utility of DBT and sDBT continues to be explored for chest, musculoskeletal, and dental imaging. Since scatter presents different challenges as the attenuation environment changes, studies exploring postacquisition processing across this spectrum will be useful as research continues to optimize tomosynthesis image presentation in general.

Disclosures

Acknowledgments

References

1. B. M. Haas et al., "Comparison of tomosynthesis plus digital mammography and digital mammography alone for breast cancer screening," *Radiology* **269**(3), 694–700 (2013).
2. E. A. Rafferty et al., "Breast cancer screening using tomosynthesis and digital mammography in dense and nondense breasts," *JAMA* **315**(16), 1784–1786 (2016).
3. S. L. Rose et al., "Implementation of breast tomosynthesis in a routine screening practice: an observational study," *Am. J. Roentgenol.* **200**(6), 1401–1408 (2013).
4. A. M. McCarthy et al., "Screening outcomes following implementation of digital breast tomosynthesis in a general-population screening program," *J. Natl. Cancer Inst.* **106**(11), dju316 (2014).
5. N. Houssami and P. Skaane, "Overview of the evidence on digital breast tomosynthesis in breast cancer detection," *Breast* **22**(2), 101–108 (2013).
6. E. S. McDonald et al., "Effectiveness of digital breast tomosynthesis compared with digital mammography: outcomes analysis from 3 years of breast cancer screening," *JAMA Oncol.* **2**(6), 737–743 (2016).
7. A.-C. Rößler et al., "Performance of photon-counting breast computed tomography, digital mammography, and digital breast tomosynthesis in evaluating breast specimens," *Acad. Radiol.* **24**(2), 184–190 (2017).
8. A. S. Tagliafico et al., "Adjunct screening with tomosynthesis or ultrasound in women with mammography-negative dense breasts: interim report of a prospective comparative trial," *J. Clin. Oncol.* **34**(16), 1882–1888 (2016).
9. D. Roganovic et al., "Breast MRI, digital mammography and breast tomosynthesis: comparison of three methods for early detection of breast cancer," *Bosnian J. Basic Med. Sci.* **15**(4), 64–68 (2015).
10. B. Batohi et al., "Comparison of MRI and digital breast tomosynthesis in the preoperative evaluation of multifocal breast cancer," *Breast Cancer Res.* **17**(Suppl. 1), P11 (2015).
11. I. Sechopoulos, "A review of breast tomosynthesis. Part I. The image acquisition process," *Med. Phys.* **40**(1), 014301 (2013).
12. L. E. Philpotts and R. J. Hooley, *Breast Tomosynthesis E-Book*, Chapter 2, Elsevier Health Sciences, Philadelphia, Pennsylvania (2016).
13. GE Medical Systems, "SenoClaire GE breast tomosynthesis clinical and non-clinical information: supplement to operator manual," p. 18, https://www.accessdata.fda.gov/cdrh_docs/pdf13/P130020c.pdf (5 December 2017).
14. R. J. Acciavatti and A. D. A. Maidment, "Optimization of continuous tube motion and step-and-shoot motion in digital breast tomosynthesis systems with patient motion," *Proc. SPIE* **8313**, 831306 (2012).
15. A. W. Tucker, J. Lu, and O. Zhou, "Dependency of image quality on system configuration parameters in a stationary digital breast tomosynthesis system," *Med. Phys.* **40**(3), 031917 (2013).
16. J. Calliste et al., "Second generation stationary digital tomosynthesis system with faster scan time and wider angular span," *Med. Phys.* **44**(9), 4482–4495 (2017).
17. C. Puett et al., "An update on carbon nanotube-enabled x-ray sources for biomedical imaging," *WIREs Nanomed. Nanobiotechnol.* **10**, e1475 (2018).
18. J. Calliste et al., "Initial clinical evaluation of stationary digital breast tomosynthesis," *Proc. SPIE* **9412**, 941228 (2015).
19. A. E. Hartman et al., "Initial clinical evaluation of stationary digital chest tomosynthesis," *Proc. SPIE* **9783**, 978366 (2016).
20. C. R. Inscoe et al., "Stationary intraoral tomosynthesis for dental imaging," *Proc. SPIE* **10132**, 1013203 (2017).
21. A. Argus and M. C. Mahoney, "Clinical indications for breast MRI," *Appl. Radiol.* **39**(10), 10–19 (2010).
22. R. A. Jong et al., "Contrast-enhanced digital mammography: initial clinical experience," *Radiology* **228**(3), 842–850 (2003).
23. M. L. Hill, J. G. Mainprize, and M. J. Yaffe, "System calibration for quantitative contrast-enhanced digital breast tomosynthesis (CEDBT)," *Lect. Notes Comput. Sci.* **9699**, 645–653 (2016).
24. L. C. Ikejimba et al., "Task-based strategy for optimized contrast enhanced breast imaging: analysis of six imaging techniques for mammography and tomosynthesis," *Med. Phys.* **41**(6), 061908 (2014).
25. L. Chen et al., "Impact of subtraction and reconstruction strategies on dual-energy contrast enhanced breast tomosynthesis with interleaved acquisition," *Proc. SPIE* **8668**, 86685O (2013).
26. C. R. Inscoe et al., "Demonstration of a scatter correction technique in digital breast tomosynthesis," *Proc. SPIE* **8668**, 86680H (2013).
27. A.-K. Carton et al., "Optimization of a dual-energy contrast-enhanced technique for a photon-counting digital breast tomosynthesis system: I. A theoretical model," *Med. Phys.* **37**(11), 5896–5907 (2010).
28. I. Sechopoulos, "X-ray scatter correction method for dedicated breast computed tomography: x-ray scatter correction for dedicated breast CT," *Med. Phys.* **39**(5), 2896–2903 (2012).
29. Y. Lu et al., "A scatter correction method for contrast-enhanced dual-energy digital breast tomosynthesis," *Phys. Med. Biol.* **60**(16), 6323–6354 (2015).
30. K. Yang, J. B. George, and J. M. Boone, "An object specific and dose-sparing scatter correction approach for a dedicated cone-beam breast CT system using a parallel-hole collimator," *Proc. SPIE* **8313**, 831303 (2012).
31. G. Wu et al., "Estimating scatter from sparsely measured primary signal," *J. Med. Imaging* **4**(1), 013508 (2017).

32. G. Wu et al., "Adapted fan-beam volume reconstruction for stationary digital breast tomosynthesis," *Proc. SPIE* **9412**, 94123J (2015).

33. C. Puett et al., "Contrast enhanced imaging with a stationary digital breast tomosynthesis system," *Proc. SPIE* **10132**, 1013225 (2017).

34. A. Woodroof, "Contrast-enhanced mammography: successful clinical experience," *Appl. Radiol.* http://appliedradiology.com/articles/contrast-enhanced-mammography-successful-clinical-experience (2018).

35. S. S. J. Feng et al., "X-ray scatter correction in breast tomosynthesis with a precomputed scatter map library," *Med. Phys.* **41**(3), 031912 (2014).

36. W. DeMartini, C. Lehman, and S. Partridge, "Breast MRI for cancer detection and characterization: a review of evidence-based clinical applications," *Acad. Radiol.* **15**(4), 408–416 (2008).

37. A. Akita et al., "The clinical value of bilateral breast MR imaging: is it worth performing on patients showing suspicious microcalcifications on mammography?" *Eur. Radiol.* **19**(9), 2089–2096 (2009).

38. R. H. El Khouli et al., "Dynamic contrast-enhanced MRI of the breast: quantitative method for kinetic curve type assessment," *AJR Am. J. Roentgenol.* **193**(4), W295–W300 (2009).

39. A. D. A. Maidment et al., "Dynamic four-dimensional contrast enhanced tomosynthesis," U.S. Patent WO 2015126504 A3 (2015).

40. Y. Z. Lee and C. M. Kuzmiak, "Comparison of stationary breast tomosynthesis and 2-D digital mammography in patients with known breast lesions," https://clinicaltrials.gov/ct2/show/NCT01773850 (5 September 2017).

41. Y. Z. Lee, "Evaluation of stationary digital breast tomosynthesis in a screening call back population and in patients with calcifications," https://oncore.unc.edu/sip/SIPControlServlet?hdn_function=SIP_PROTOCOL_SUMMARY&protocol_no=LCCC1414 (5 September 2017).

Biographies for the authors are not available.